JOURNAL OF GEOPHYSICAL RESEARCH, VOL. 113, D11108, doi:10.1029/2007JD009231, 2008

An observing system simulation experiment for climate monitoring with GNSS radio occultation data: Setup and test bed study

Ulrich Foelsche,[1,2] Gottfried Kirchengast,[1,2] Andrea K. Steiner,[1,2] Luis Kornblueh,[3] Elisa Manzini,[4] and Lennart Bengtsson[3]

Received 28 July 2007; revised 22 January 2008; accepted 11 February 2008; published 6 June 2008.

[1] The long-term stability, high accuracy, all-weather capability, high vertical resolution, and global coverage of Global Navigation Satellite System (GNSS) radio occultation (RO) suggests it as a promising tool for global monitoring of atmospheric temperature change. With the aim to investigate and quantify how well a GNSS RO observing system is able to detect climate trends, we are currently performing an (climate) observing system simulation experiment over the 25-year period 2001 to 2025, which involves quasi-realistic modeling of the neutral atmosphere and the ionosphere. We carried out two climate simulations with the general circulation model MAECHAM5 (Middle Atmosphere European Centre/Hamburg Model Version 5) of the MPI-M Hamburg, covering the period 2001–2025: One control run with natural variability only and one run also including anthropogenic forcings due to greenhouse gases, sulfate aerosols, and tropospheric ozone. On the basis of this, we perform quasi-realistic simulations of RO observables for a small GNSS receiver constellation (six satellites), state-of-the-art data processing for atmospheric profiles retrieval, and a statistical analysis of temperature trends in both the ''observed'' climatology and the ''true'' climatology. Here we describe the setup of the experiment and results from a test bed study conducted to obtain a basic set of realistic estimates of observational errors (instrument- and retrieval processing-related errors) and sampling errors (due to spatial-temporal undersampling). The test bed results, obtained for a typical summer season and compared to the climatic 2001–2025 trends from the MAECHAM5 simulation including anthropogenic forcing, were found encouraging for performing the full 25-year experiment. They indicated that observational and sampling errors (both contributing about 0.2 K) are consistent with recent estimates of these errors from real RO data and that they should be sufficiently small for monitoring expected temperature trends in the global atmosphere over the next 10 to 20 years in most regions of the upper troposphere and lower stratosphere (UTLS). Inspection of the MAECHAM5 trends in different RO-accessible atmospheric parameters (microwave refractivity and pressure/geopotential height in addition to temperature) indicates complementary climate change sensitivity in different regions of the UTLS so that optimized climate monitoring shall combine information from all climatic key variables retrievable from GNSS RO data.

Citation: Foelsche, U., G. Kirchengast, A. K. Steiner, L. Kornblueh, E. Manzini, and L. Bengtsson (2008), An observing system simulation experiment for climate monitoring with GNSS radio occultation data: Setup and test bed study, *J. Geophys. Res.*, *113*, D11108, doi:10.1029/2007JD009231.

1. Introduction

[2] The provision of accurate, long-term consistent data to sustain and expand the observational foundation for climate studies is one of the high priority areas for action to improve the ability to detect, attribute and understand climate variability and change [*IPCC*, 2007]. While there is little doubt that the Earth's surface temperature has risen by at least 0.6°C during the 20th century [*IPCC*, 2001, 2007; *Trenberth et al.*, 2007], our knowledge about temperature trends in the free atmosphere is still limited.

[3] Upper air records have been built using data from radiosondes [e.g., *Sherwood et al.*, 2005; *Thorne et al.*,

[1]Wegener Center for Climate and Global Change (WegCenter), University of Graz, Graz, Austria.
[2]Institute for Geophysics, Astrophysics, and Meteorology (IGAM), University of Graz, Graz, Austria.
[3]Max-Planck-Institute for Meteorology (MPI-M), Hamburg, Germany.
[4]Istituto Nazionale di Geofisica e Vulcanologia (INGV) and Centro Euro-Mediterraneo per il Cambiamento Climatico, Bologna, Italy.

0148-0227/08/2007JD009231$09.00

2005]. These data cover almost five decades but they are concentrated in the continental regions of the Northern Hemisphere and suffer from problems like changes in instrumentation and processing or solar heating of the sensors during daytime [*Sherwood et al.*, 2005]. As a consequence no single data product has emerged yet as a generally recognized reference [*Seidel et al.*, 2004].

[4] Conventional satellite derived data records like those from the microwave sounding units (MSU) and AMSU (Advanced MSU) on board NOAA polar orbiting satellites are degraded by problems like instrument and orbit changes, calibration problems, instrument drifts, and insufficient vertical resolution [*Anthes et al.*, 2000]. Because of these shortcomings, the amount of temperature trends in the free atmosphere has been under considerable debate for many years [e.g., *Christy and Spencer*, 2003; *Vinnikov and Grody*, 2003; *Mears et al.*, 2003; *Fu et al.*, 2004; *Bengtsson et al.*, 2004; *Mears and Wentz*, 2005; *Vinnikov et al.*, 2006]. After intense discussions, temperature trend estimates based on these data sets now seem to be consistent with surface warming estimates and results from climate models but significant discrepancies still remain [*Karl et al.*, 2006]. Additional and independent high-quality upper air records are therefore required.

[5] The Global Navigation Satellite System (GNSS) radio occultation (RO) technique has the potential to substantially contribute to this scientific challenge [e.g., *Leroy and North*, 2000; *Borsche et al.*, 2007; *Foelsche et al.*, 2007; *Steiner et al.*, 2007]. With respect to climate studies, one of the most important properties of the RO technique is the expected long-term stability of RO data. It is achieved since precise atomic clocks are the basis for accurate measurements during each single occultation event, independent of whether two events are separated by an hour or by decades.

[6] We are currently performing a large-scale climate observing system simulation experiment (OSSE) over a 25 year period, which aims at testing the climate trends detection capability of GNSS RO sensors. In this study we present the OSSE setup and results from a test bed study, based on an example season, including a detailed error analysis. In section 2 we shortly review the basic principles of GNSS RO with focus on the properties enabling accurate climate monitoring. Section 3 introduces the climate OSSE setup. The detailed results of the test bed study are presented in section 4 and their comparison to expected trends as well as the utility for trend detection of inspecting different RO-accessible atmospheric parameters is addressed in section 5. Section 6, finally, provides a summary, conclusions, and an outlook to analyzing the complete OSSE.

2. GNSS Radio Occultation

2.1. Principles and Missions

[7] GNSS RO observations are performed in an active limb sounding mode, vertical scanning is provided by the relative motion of a GNSS transmitter and a Low-Earth-Orbit (LEO) receiver satellite. From the viewpoint of the receiver in LEO, an occultation event occurs when the transmitting GNSS satellite passes across the atmospheric limb and the GNSS radio signals traverse the atmosphere and ionosphere, whereby they are refracted. Observed excess phases (relative to propagation in vacuum) can be accurately measured and are the basis for high quality retrievals of bending angle profiles and, subsequently, profiles of the atmospheric variables: refractivity, density, pressure, geopotential height, temperature, and humidity (see section 3.5). For a detailed description of the GNSS RO technique see, e.g., the reviews of *Kursinski et al.* [1997], *Steiner et al.* [2001], and *Hajj et al.* [2002].

[8] The RO technique in general was first applied to planetary atmospheres (see *Yunck et al.* [2000] for a review); accurate sensing of the Earth's atmosphere became feasible with the precise signals of the GPS (Global Positioning System) satellites, as successfully demonstrated with the U.S. GPS/MET experiment [e.g., *Ware et al.*, 1996; *Rocken et al.*, 1997; *Steiner et al.*, 1999]. Data from the German CHAMP satellite (Challenging Minisatellite Payload) provided the first opportunity to create multiyear RO based climatologies [*Foelsche et al.*, 2005, 2007]. Continuous measurements started in 2001 [e.g., *Wickert et al.*, 2004] and the satellite is still active (expected until end of 2008). FORMOSAT-3/COSMIC (Constellation Observing System for Meteorology, Ionosphere, and Climate), a Taiwan/U.S. RO mission consisting of six receiving satellites [*Rocken et al.*, 2000; *Wu et al.*, 2005], was successfully launched in April 2006 and started by mid 2006 to provide up to ~2500 RO profiles per day [*Liou et al.*, 2007; *Schreiner et al.*, 2007]. In October 2006, MetOp-A was launched as the first of three almost identical MetOp satellites, each equipped with the same GNSS Receiver for Atmospheric Sounding (GRAS) [*Loiselet et al.*, 2000; *Luntama*, 2006]. This European MetOp/GRAS mission is the first to provide operational RO measurements over about 15 years (until 2020) with essentially the same instrument. A rich RO database for climate applications seems thus assured.

2.2. Climate Monitoring

[9] The special climate monitoring utility of RO data arises from the fact that atmospheric profiles are not derived from absolute values (phase delays) but from Doppler shift (phase change) profiles. Therefore RO measurements require no external calibration and only short-term measurement stability over the occultation event duration (1–2 min), which is provided by very stable oscillators onboard the GNSS satellites (potential residual GNSS clock errors and clock errors on the receiving satellites can be corrected by relating the measurements to even more stable oscillators on the ground [*Hajj et al.*, 2002]). Given this "self-calibration", data from different sensors and different occultation missions can be combined without need for intercalibration and overlap, provided that the same data processing scheme is used and spatiotemporal sampling [*Pirscher et al.*, 2007] is well understood.

[10] The potential of RO data for climate monitoring has been shown with simulation studies [e.g., *Yuan et al.*, 1993; *Steiner et al.*, 2001; *Foelsche et al.*, 2003; *Leroy et al.*, 2006a, 2006b]. RO records have been successfully validated against (A)MSU data [*Schrøder et al.*, 2003; *Steiner et al.*, 2007], climatological analyses [*Gobiet et al.*, 2005, 2007; *Foelsche et al.*, 2006, 2007], RO data from different satellites [*Hajj et al.*, 2004; *Foelsche et al.*, 2008], and against data from MIPAS (Michelson Interferometer for

Passive Atmospheric Sounding) and GOMOS (Global Ozone Monitoring for Occultation of Stars) on Envisat [*Gobiet et al.*, 2007]. The utility of RO data for monitoring tropopause parameters has been shown by *Schmidt et al.* [2005, 2006] and *Borsche et al.* [2007].

3. Observing System Simulation Experiment

[11] In numerical weather prediction as the classical OSSE domain, OSSEs are performed to assess the impact of a future or hypothetical data type on a forecast system (for an instructive introduction, not well available in literature, see, e.g., http://sivo.gsfc.nasa.gov/OSSE/). In the present "climate OSSE" we aim at assessing the capability of a future observing system (long-term GNSS RO data set) to detect climate change. In contrast to real atmospheric measurements, where the "true" state is always unknown, an OSSE allows for comparison with the "truth". The present study is based on an end-to-end forward-inverse simulation. In the forward simulations, the OSSE comprises modeling of the neutral atmosphere and ionosphere, geometrical simulation of the GNSS RO events, and forward modeling of excess phase observables including trans-atmospheric and -ionospheric signal propagation and quasi-realistic observation system error modeling, respectively. In the inverse simulations, it comprises the retrieval processing chain from the RO (excess phase) observables to the retrieved atmospheric profiles, in particular temperature profiles. An initial design of this study has been presented by *Kirchengast et al.* [2000] and *Steiner et al.* [2001], initial results summarized by *Foelsche et al.* [2003]. The forward-inverse simulations are performed with a study-tailored version of the End-to-end GNSS Occultation Performance Simulator (EGOPS) software tool [*Kirchengast et al.*, 2002]. We sequentially describe the main components of the OSSE end-to-end simulations setup in sections 3.1–3.5 below.

3.1. Atmospheric Modeling

[12] In order to obtain reliably simulated RO data, it is of particular importance to use adequate models of the neutral atmosphere and the ionosphere, the latter for proper capturing of ionospheric residual errors in retrieved atmospheric profiles, which are an important part of the error budget from about 30 km upwards [e.g., *Kursinski et al.*, 1997; *Gobiet and Kirchengast*, 2004; *Steiner and Kirchengast*, 2005].

[13] For the test bed study season (summer 1997; details see section 4) we modeled the neutral atmosphere with the General Circulation Model ECHAM4 (European Centre/Hamburg Model) [*Roeckner et al.*, 1999] in Middle Atmosphere mode (MAECHAM4) with a resolution of T42L39 [*Manzini and McFarlane*, 1998; *Manzini et al.*, 1997]. The triangular truncation at wave number 42 corresponds to a horizontal resolution of ~300 km, approximately matching the horizontal resolution of RO profiles. The highest of the 39 model levels is located at ~0.01 hPa or ~80 km. Above 70 km we used a smooth transition to MSISE-90 climatology fields [*Hedin*, 1991]. This coverage of the full stratosphere and stratopause region up into the mesosphere is essential to get realistic atmospheric variability at initialization heights of RO retrieval [*Gobiet and Kirchengast*, 2004]. The climate model fields are stored every 6 h, ensuring that the subsequent simulation of RO observables can capture diurnal to decadal variations.

[14] Given the recent improvements in atmospheric modeling, we decided for the full 25-year experiment 2001–2025 to use MAECHAM5, the successor of the MAECHAM4 model, again at T42L39 resolution. MAECHAM5 [e.g., *Manzini et al.*, 2006; *Giorgetta et al.*, 2006] is able to simulate middle atmosphere variability in a fairly realistic manner. After successful completion of a control run, a forced model run for the time period 2001 to 2025 including transient anthropogenic forcings due to greenhouse gases, sulfate aerosol, and ozone has been performed at the MPI-M Hamburg, Germany. The underlying emission scenario is IS92a [e.g., *IPCC*, 2001], initial and boundary conditions (e.g., sea surface temperature) of this time-slice simulation are from a long-time integration of the ECHAM4 model at T42L19 resolution (using the same emission scenario), coupled with the OPYC ocean model [*Roeckner et al.*, 1999; *Bengtsson et al.*, 1999]. IS92a is characterized by comparatively high sulfur emissions and intermediate CO_2 emissions, leading to a projected atmospheric CO_2 concentration of about 700 ppm in 2100. The projection for the globally averaged surface temperature in 2100 is about 2.5 K above the 1990 value [*IPCC*, 2001]. The simulated changes in the neutral atmosphere can therefore be considered relatively conservative estimates of the future evolution. However, due to the inertia in the climate system, near-future climate change projections until 2025 are anyway weakly dependent on the specific emission/concentration scenario [*IPCC*, 2001, 2007].

3.2. Ionospheric Modeling

[15] Regarding climate monitoring, potential decadal scale variability of residual ionospheric systematic errors is of particular importance, since it could pretend short-term trends in RO climatologies of the stratosphere. It is therefore essential to account for the ~11 year solar cycle in modeling the ionosphere, in order to get simulated RO measurements with realistic error characteristics. For this purpose we used the NeUoG (Electron Density, University of Graz) model [*Leitinger et al.*, 1996; *Leitinger and Kirchengast*, 1997], a global empirical climatology for the 3D ionospheric electron density field, which has been of good use in several other occultation-related studies [e.g., *Leitinger and Kirchengast*, 1997; *Gobiet and Kirchengast*, 2004; *Steiner and Kirchengast*, 2005]. It is driven by day-to-day variations of the solar activity (including the ~11 year solar cycle), represented by the F10.7 solar flux index. The Solar Flux at 10.7 cm wavelength is given in solar flux units (1 sfu = 10^{-22} $Wm^{-2}Hz^{-1}$). We downloaded past F10.7 values from the National Geophysical Data Center (http://ngdc.noaa.gov/stp/SOLAR/ftpsolarradio.html) and used data from the solar cycles 21, 22, and 23 to mimic reasonable solar activity variations for the time period 2004 to 2025 (using the real data until 2003).

[16] "Weekly history averages" (averages over 7 d up to and including the current day) are a good proxy for sun-induced ionospheric variations; we used these values as input for the NeUoG model. The computed weekly history averages and monthly mean values for the period 1996 to 2025 are displayed in Figure 1. F10.7 values for the test bed

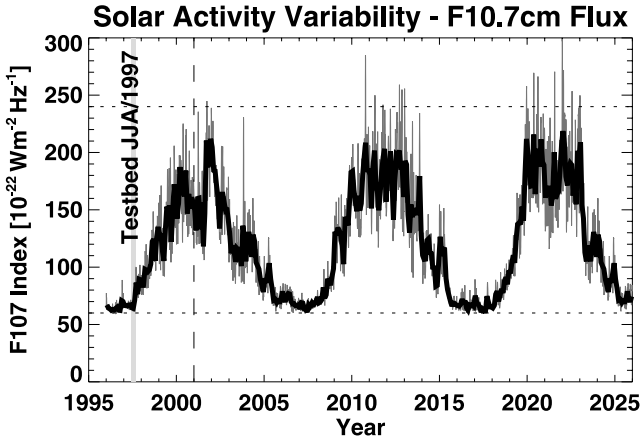

Figure 1. Solar activity variability represented by F10.7 flux values: "Weekly history averages" (grey) and monthly mean values (black).

season (JJA 1997) range from 60 to 80, the test bed results are therefore representative for low solar activity.

[17] The NeUoG model does not account for small-scale irregularities. To roughly compensate for this, we increased the random errors superimposed to RO phase delay profiles to generate simulated measurements with a reasonable noise level (see section 3.4). With our simulation of ionospheric effects we well capture the bulk effects related to changes of electron density over the solar cycle (and not entirely removed by ionospheric correction; see section 3.5). Ionospheric errors during strong magnetic storms or caused by sharp inclined sporadic E-layers [e.g., *Pavelyev et al.*, 2007] are certainly larger, but they occur only intermittently in space and time and should not degrade climatological averages.

3.3. Simulation of RO Observables and Domain Selection

[18] We assumed a small constellation of six LEO satellites equipped with GNSS receivers, comparable to planned and recently launched RO missions, such as ACE+ [*Hoeg and Kirchengast*, 2002] and FORMOSAT-3/COSMIC [*Wu et al.*, 2005; *Liou et al.*, 2007; *Schreiner et al.*, 2007].

[19] The LEO satellites (LEOs) are placed in two orbit planes, separated in their equatorial nodes by 90°, with four LEOs in a high inclination orbit ($i = 80°$) and two LEOs in a low inclination orbit ($i = 30°$), respectively. All LEOs have an orbit height of about 850 km and are equipped with fore- and aft-looking antennas, enabling the reception of rising and setting RO events, respectively. For the entire 25 year simulation we assumed five identical consecutive LEO constellations with a lifetime of five years each (following, in terms of lifetime cycle, the MetOp/GRAS mission, which comprises a sequence of three satellites, MetOp-A, -B, -C, each with a 5-year lifetime).

[20] The GNSS currently consists of the U.S. GPS and the Russian GLONASS (Global'naya Navigatsionnaya Sputnikovaya Sistema) with nominal constellations of 24 satellites each. A European system with nominally 30 additional satellites (Galileo) is currently set up and scheduled to be operational by 2012. For the test bed study we used nominal constellations of GPS and GLONASS as transmitting satellites (in combination with LEO receivers which can track signals from both constellations). Given the recent Galileo activities and the future of GLONASS perceived less clear, we decided to assume nominal constellations of GPS and Galileo for the 25-year OSSE. The geometrical data for each RO event are calculated based on Keplerian orbits for the respective transmitting and receiving satellites, resulting in realistic locations of the RO events in space and time.

[21] Considering that RO events with a high angle of incidence (azimuth angle) with respect to the LEO orbit plane are more vulnerable to horizontal variability errors, we conservatively restricted for the test bed study to occultations within ±15° about the LEO orbit plane (near-vertical events). Following *Foelsche and Kirchengast* [2004] this conservative setting to safeguard the climate quality of RO data is not needed above ~7 km altitude, since no relevant increase of errors with increasing angle of incidence has been detected above 7 km. Therefore we relaxed this restriction for the full 25-year run, allowing for occultations within ±30° about the LEO orbit plane. With this setup a more even space-time distribution of RO events can be reached.

[22] Even with the conservative ±15° azimuth restriction, the selected LEO constellation yields about 2000 rising and setting occultations per day (or more then 18 million within a 25-year period), with nominal GPS and GLONASS constellations. In order to reduce computation time we had to extract a small but sensible subset of these RO events because the high-precision simulation of observables of a single RO event consumes several hours on a typical workstation processor, mainly for the trans-atmospheric and -ionospheric signal propagation modeling by full 3D ray tracing, which is required for the realism of the OSSE, however.

[23] In terms of space-time domain, we focus on the (northern) summer season (June, July, August) and on a geographic domain between 85°S and 85°N, symmetric with respect to the Greenwich meridian and divided into 17 equal area "bins" (15° longitude × 10° latitude at Equator). Figure 2a shows a geographic map with the selected domain in which about 13,000 RO events can be expected within a summer season, for six LEO receivers and the setup described above. In a further step to make the study computationally feasible, we restricted the OSSE to a sample size of about 1000 events per summer season with an approximately uniform distribution in time and latitude, yielding 50 to 60 events per latitude bin. The locations of the selected events during the JJA 1997 test bed season are shown in Figure 2a and the monthly and seasonal latitudinal distribution in Figure 2b, respectively.

[24] For each of the selected RO events we performed 3D ray tracing with submillimetric accuracy at 10 Hz sampling rate through the respective atmospheric and ionospheric fields, providing signal phase delay profiles as seen by a RO sensor. These computations have been performed with a special node-parallelized version of the forward modeling part of the EGOPS tool, employing its 3D ray tracer developed by *Syndergaard* [1999].

[25] Since ray tracing, based on geometric optics, stops at multipath situations in the lower troposphere, when sharp vertical refractivity gradients are encountered, the simulations do not account for multipath and diffraction effects

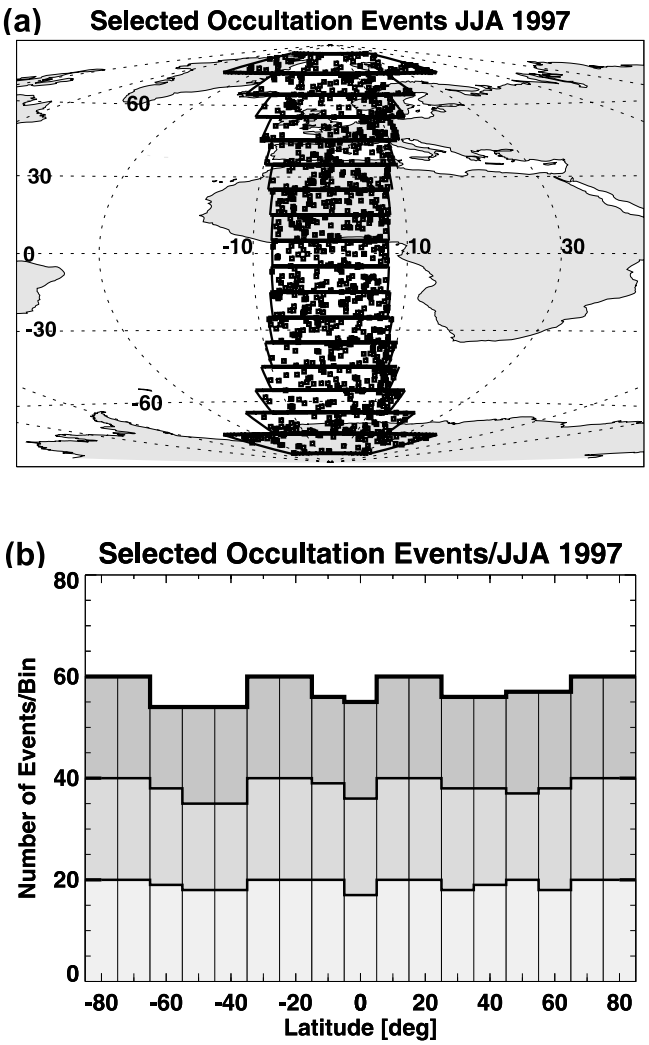

Figure 2. (a) Geographical domain and distribution of the ~1000 selected occultation events (squares) in 17 equal area bins for the season JJA 1997 (Hammer-Aitoff equal area projection). (b) Cumulative distribution of the selected events in the 17 bins in June (light grey), June + July (plus medium grey), and June + July + August (plus dark grey).

[e.g., *Gorbunov*, 2002; *Jensen et al.*, 2003; *Gorbunov and Lauritsen*, 2004]. An advantage of the ray tracing approach is its ease of use for propagating through combined atmospheric and ionospheric fields while forward modeling based on wave optics could clearly provide better results in the lower troposphere. As we focus on the UTLS (upper troposphere and lower stratosphere), and do not intend to interpret results below 8 km in detail, we decided to use the ray tracing approach.

3.4. Superposition of Errors

[26] In a last step to simulate the RO observables, we superimposed typical instrumental and raw processing system errors on the simulated phase delay profiles obtained from the signal propagation modeling. For this purpose we used values somewhat above the error specifications of the MetOp/GRAS receiver [*Luntama*, 2006; *Steiner and Kirchengast*, 2005], considering that this receiver provides a sensible (and not overoptimistic) example for future RO receiving systems.

[27] Modeling of the observation system includes precise orbit determination (POD) errors, antenna pattern, local multipath, receiver thermal noise, and clock instabilities. The POD error model contains satellite positioning and velocity errors (modeled randomly based on specified standard errors), where the along-ray velocity standard error of 0.05 mm/s, typical for modern POD systems, is the dominant error source. The radial position standard errors of the LEO and the GNSS satellites were set to 0.4 m and 0.2 m, respectively, a conservative bound for modern POD performance. Receiver noise was modeled as white Gaussian noise with a LEO antennae noise temperature of 250 K and a (single-side) tracking loop bandwidth of 10 Hz. The antenna noise temperature of 250 K is significantly higher than a realistic value for the GRAS receiver (near 150 K) in order to get increased thermal noise to account for missing ionospheric noise from small-scale irregularities in the simulated measurements (section 3.2). For the 25-year experiment we consider to let this additional "proxy ionospheric noise" vary as a function of F10.7 (Figure 1) to roughly account also for its time variation depending on solar activity level.

[28] Local multipath was modeled using a sinusoidal function with a multipath phase error period of 100 s and an amplitude of 1 mm, with random phase of the sine function from event to event. This error is a proxy for the typical local multipath effect of inducing small periodic phase errors with periods of the order of the occultation event duration (though on well designed receiver platforms they are clearly smaller than modeled here). It is at the same time a reasonable proxy for potential residual drift errors in RO data. Regarding clock errors, we modeled these based on a random-walk model and assuming a ground-based single differencing clock correction method (see, e.g., *Hajj et al.* [2002], for details on differencing and clock correction methods), setting the stability of the ground clock to a 1-s Allan deviation of $1 \cdot 10^{-13}$. This modeling is representative for the performance of high-quality ultra-stable oscillators as used in modern GNSS RO observing system setups.

[29] A detailed error analysis for an ensemble of 300 simulated RO profiles, using essentially the same error characteristics as chosen for this OSSE study, but European Centre for Medium-Range Weather Forecasts (ECMWF) fields for the forward modeling, is given by *Steiner and Kirchengast* [2005]. That study showed how these phase delay observation errors propagate through an RO retrieval chain into the retrieved atmospheric profiles.

3.5. Retrieval of Atmospheric Parameters

[30] The excess phase profiles are inverted to profiles of atmospheric parameters using a retrieval processing chain described by *Steiner and Kirchengast* [2005], which is an enhanced version of the algorithm described by *Syndergaard* [1999]. Briefly, the phase delay data are filtered with a regularization method resembling a low-pass filter to eliminate high frequency noise. Doppler shift data, obtained by time-derivation of the filtered phase data, are the basis for the computation of bending angle profiles. We applied the ionospheric correction at bending angle level, which leads to a considerably smaller residual bias in derived

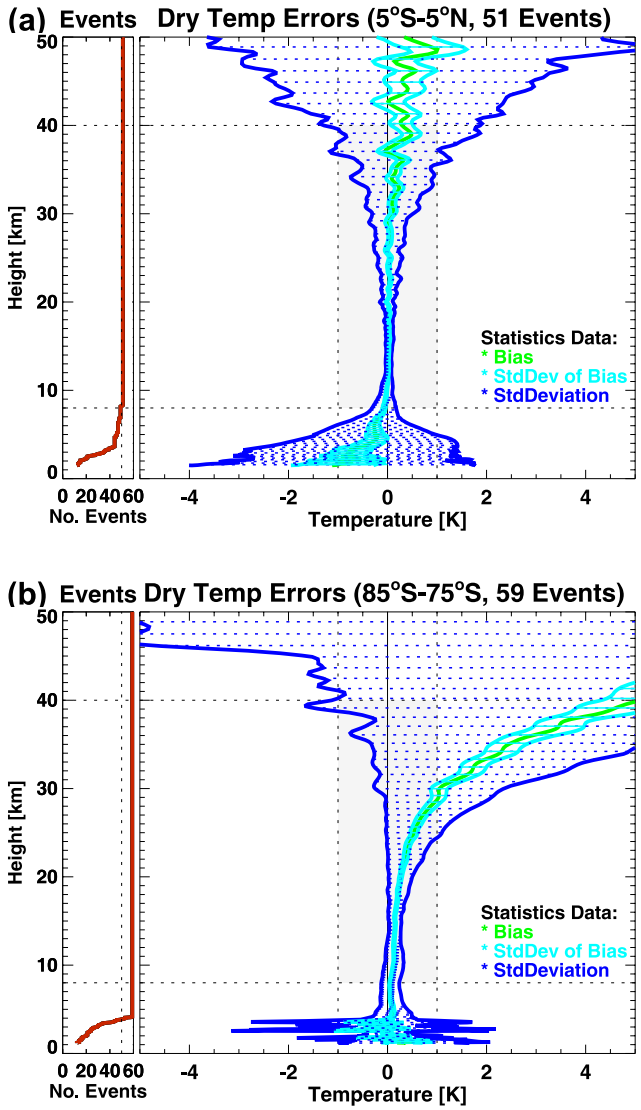

Figure 3. Temperature error statistics during the JJA 1997 season for (a) the equatorial bin and (b) the southernmost bin: number of ensemble members (red, left side-panels), bias (green), uncertainty of the bias (turquoise), and standard deviation (blue). The "core region" (8 to 40 km) is indicated by dotted lines and, within that, the ±1 K range by shading.

bending angles than the phase correction method [*Vorob'ev and Krasil'nikova*, 1994; *Gobiet and Kirchengast*, 2004].

[31] The bending angle measurement error was estimated as the standard deviation of the observed bending angle profile at mesospheric heights between 70 and 80 km, where the bending angle signal is small and ionospheric residuals and measurement noise dominate. The average standard error of the retrieved bending angles is about 1.2 μrad, slightly larger than the accuracy requirement specification of 1 μrad of the MetOp/GRAS operational RO receiving system [*Luntama*, 2006]. This observation error is also used as quality criterion, all events with an error >4 μrad and events which are beyond the "3σ-limit" in the respective latitude bin are interpreted as outliers and excluded from statistics, which typically affects 1–4 events per bin.

[32] Refractivity, density, pressure, geopotential height, and dry temperature profiles are calculated from the bending angle profiles by using a classical GNSS RO retrieval chain, summarized by *Gobiet and Kirchengast* [2004]. The step from bending angles to refractivities involves an inverse Abel transform [*Fjeldbo et al.*, 1971]. Since its upper integration limit ranges to infinity, the inverse Abel transform needs some kind of high-altitude initialization of the bending angle profile. This is done with background bending angles derived from the MSISE-90 climatology [*Hedin*, 1991]. A library search within the full lat/lon/month model domain in the height interval of 40–65 km is performed to find the best fitting background bending angle profile, using a least squares criterion. An inverse covariance-weighting statistical optimization is applied to combine observed and background bending angle profiles as described in detail by *Gobiet and Kirchengast* [2004].

[33] Temperature profiles are derived from refractivity profiles, based on standard formulae [e.g., *Kursinski et al.*, 1997], assuming a dry atmosphere. Refractivity at microwave frequencies depends on temperature and water vapor [*Smith and Weintraub*, 1953]. Neglecting water vapor yields "dry temperature", a parameter which is commonly used in the RO community. In the presence of water vapor, dry temperature is always colder than physical temperature. At altitudes above 8 km (polar winter) and 14 km (tropics), however, this difference is always well below 0.1 K. A detailed discussion is given by *Foelsche et al.* [2007]. In the following we generally compare retrieved RO dry temperature profiles to "true" dry temperature profiles from the GCM model.

4. Results From the Test Bed Study

4.1. Ensemble Error Statistics

[34] For each "measured" RO profile we extracted a colocated vertical GCM profile from the nearest time layer at the mean location of the (nonvertical) RO profile, using spatial interpolation. We define the mean location as the latitude and longitude of the point, where the straight-line connection between transmitting and receiving satellite during the occultation event touches the Earth's ellipsoidal surface (corresponding to the tangent point location of real RO profiles at about 12 to 15 km altitude).

[35] Differences between retrieved dry temperature profiles and colocated "true" GCM dry temperature profiles have been computed for the set of 50–60 events in each of the 17 latitude bins with 10° latitudinal extent, allowing the inspection of systematic and random observational errors. Results of these "difference error statistics" for two bins during the test bed season JJA 1997 are shown as examples in Figure 3. The mean of the difference profiles is the bias of the ensemble. We primarily focus on a "core region" between 8 and 40 km height where the best results can be expected.

[36] The equatorial bin (5°S to 5°N) is a typical case with small biases (<0.1–0.5 K) everywhere in the core region (Figure 3a), confirming the high precision and accuracy of RO measurements in the upper troposphere and lower stratosphere [e.g., *Schreiner et al.*, 2007]. The ensemble is

essentially bias-free between 10 and 30 km height, standard deviations are smaller than 1 K between 6 km and 37 km height. With ~50–60 events in each bin (note that the numbers are smaller than in Figure 2b due to outlier rejection), the standard deviation of the mean (bias) is by about a factor of seven smaller than the standard deviation of the ensemble. The decrease of the number of ensemble members with decreasing height (left side-panel of Figure 3a) is due to the fact that the ray tracer stops when severe multipath or superrefractive structures are encountered (in case of superrefraction, ray bending is so strong that the ray hits the Earth's surface). This situation is frequently encountered in the lower tropical troposphere, where large variations of the water vapor content lead to sharp vertical refractivity gradients [e.g., *Kursinski et al.*, 1997].

[37] The southernmost bin (85°S to 75°S) is the "worst case", mainly due to weak representativity of the MSIS-90 climatology there (Figure 3b) [*Gobiet and Kirchengast*, 2004; *Steiner and Kirchengast*, 2005]. The Antarctic winter stratosphere is so cold that no adequate background bending angle profiles can be found by the MSIS library search algorithm (section 3.5). The best fitting background profiles are therefore too warm, mapping into a warm bias of the RO profiles ensemble. Systematic and statistical errors <1 K can only be found between 4 and 28 km height. A similar, but less severe situation is encountered in the 75°S to 65°S bin. The bias structure seen in Figure 3b thus illustrates the importance of proper initialization of the bending angle profile, as well as the downward propagation of systematic errors, when the background is severely biased.

[38] This situation, at southern polar latitudes, can be expected to worsen for the 25 year experiment, given the projected stratospheric cooling over this time period (see section 5). Therefore while at first sight the approach of high altitude initialization with (static) background climatology might seem sufficient, it would leave a time-varying bias at high altitudes and cannot be recommended for climatological applications.

[39] For the full 25-year run we will thus use a further enhanced initialization, including MSIS library search plus background bias correction following *Gobiet and Kirchengast* [2004]. The result profile of the MSIS library search is in this case additionally adjusted by multiplying it with a fitting coefficient (a factor usually close to unity) derived from regression with respect to the observed profile at high altitudes (least squares adjustment). This approach leads to systematic errors <1 K everywhere below 40 km, but we prefer to show the results obtained without background bias correction since they nicely illustrate the potential problems caused by initialization with climatology. For actual RO climatologies [*Foelsche et al.*, 2007] we use ECMWF (European Centre for Medium-Range Weather Forecasts) analyses to provide background profiles (and forecasts, after the start of the assimilation of RO data in December 2006). These background data are significantly closer to the "truth" than climatological fields, but they are clearly not available for the 25-year simulation experiment.

[40] Regarding the tropospheric penetration of RO events at high latitudes, they frequently reach down to near the surface as the air is cold and dry and multipath/superrefraction is rare. The sharp decrease of ensemble members with decreasing height (left side-panel of Figure 3b) at these latitudes is mainly due to the orography of Antarctica in the respective bin (in T42 horizontal resolution). Only few profiles penetrate below 3 km height, the remaining ensemble shows high variability.

4.2. Dry Temperature Climatology

[41] The computation of climatologies and the estimation of the respective errors follow the approach used for RO climatologies from the CHAMP satellite, described by *Foelsche et al.* [2007], i.e., the climatologies are obtained by "binning and averaging". All "observed" dry temperature profiles in a prescribed bin are sampled and averaged (weighted by the cosine of the latitude), using a common altitude grid. The mean dry temperature profile in each of the 17 bins (see Figure 2a) is given by

$$\overline{T_{\mathrm{dry}}(z)} = \frac{1}{\sum_{i=1}^{N_{\mathrm{prof}}(z)} \cos(\varphi_i)} \sum_{i=1}^{N_{\mathrm{prof}}(z)} T_{\mathrm{dry}_i}(z, \varphi_i) \cos(\varphi_i), \qquad (1)$$

where N_{prof} is the number of profiles in each bin, which decreases with decreasing height in the troposphere (see section 4.1). At this latitudinal resolution the effect of cosine-weighting in equation (1) is very small, but it would start to be relevant for larger-area averages.

[42] In the vertical we compute mean values for 34 vertical layers between 2 km and 50 km altitude, corresponding approximately to the physical resolution of the retrieval. The vertical extent of the layers is 1 km between 2 km and 15 km altitude, 1.5 km between 15 km and 30 km altitude, and 2 km between 30 km and 50 km altitude, yielding a JJA mean temperature field in form of a 17 bins × 34 layers matrix. The same is done for the "true" colocated profiles. For comparison, a "true" JJA climatology matrix is computed, on the same grid, directly from sampling the complete 3D GCM dry temperature field. The RO-derived dry temperature climatology for JJA 1997 is displayed in Figure 4a, showing prominent features like the cold tropical tropopause region and the cold austral polar vortex during southern winter. Visible differences between dry and physical temperatures (not shown) occur in the lower troposphere, where the former do not reach values above 280 K while a steady increase of the latter with decreasing height would occur. For comparison, the "true" dry temperature climatology derived from the full 3D GCM grid is shown in Figure 4b, which is evidently closely matched by the retrieved climatology (Figure 4a).

4.3. Systematic Error and Observational Error

[43] The total error of RO climatologies can be separated into an observational component and a sampling error component, the latter due to incomplete sampling of the full spatial and temporal variability [*Foelsche et al.*, 2006, 2007; *Pirscher et al.*, 2007]. The dry temperature bias on the 17 × 34 grid is displayed in Figure 5a; it is the difference between the field shown in Figure 4a and the corresponding field computed from "true" colocated profiles. We have deliberately chosen nonequidistant contours to better highlight also small differences. The bias profiles in Figure 3 correspond to vertical cuts through the contours

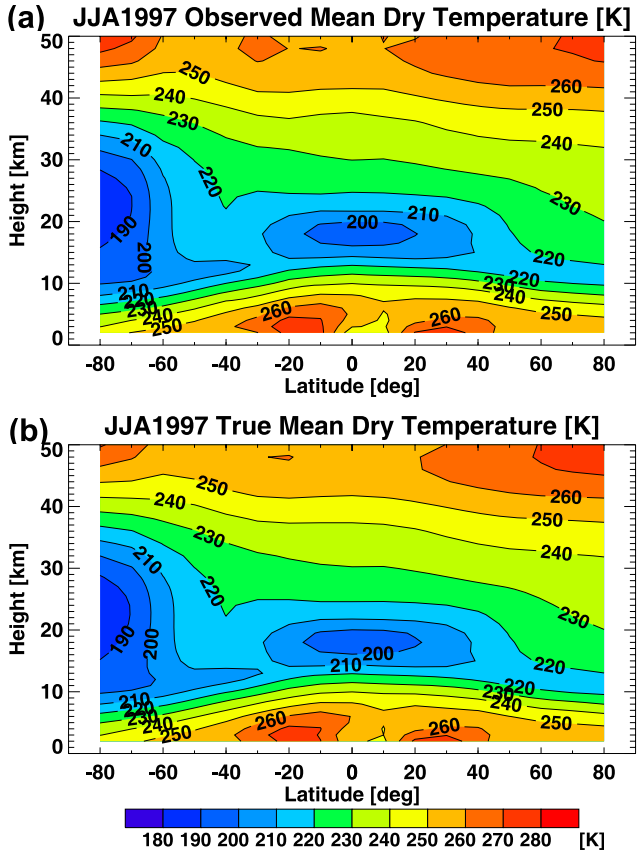

Figure 4. (a) Observed (RO-derived) dry temperature climatology for JJA 1997. (b) "True" GCM dry temperature climatology for JJA 1997.

in Figure 5a at 0° and 80°S latitude, respectively (with different height resolution). In large parts of the core region (between 8 km and 40 km altitude, indicated with dashed lines) the bias is <0.1 K. The mean absolute bias in the complete core region (as a typical value) is 0.21 K (0.15 K in the Northern Hemisphere), dominated by the contributions above 30 km. Higher values in the Southern Hemisphere are primarily due to the high altitude initialization error in the three southernmost latitude bins. The approach of MSIS library search plus background bias correction (section 4.1) essentially eliminates the large systematic errors in the core region south of 60°S [*Gobiet and Kirchengast*, 2004]. Systematic errors of more than 1 K are then restricted to altitudes above 40 km and systematic errors in the core region are approximately equal in both hemispheres. Nevertheless, we prefer to show here the results for bending angle optimization without background bias correction, since they are more illustrative, but we note that we interpret the results for the Northern Hemisphere as more representative.

[44] The systematic error of actual RO climatologies can currently not be determined to a level below 0.2–0.5 K, mainly due to limitations in the available validation data [*Foelsche et al.*, 2007; *Gobiet et al.*, 2007]. An intersatellite comparison study by *Hajj et al.* [2004] based on data from CHAMP and SAC-C (Satélite de Aplicaciones Científicas-C), however, showed a remarkable consistency of the RO data obtained from these two different satellites, with temperature profiles found consistent to within 0.1 K in the mean between 5 km and 15 km. First results on RO climatologies from FORMOSAT-3/COSMIC [*Foelsche et al.*, 2008] indicate excellent agreement between RO climatologies from different COSMIC satellites as well as between data from

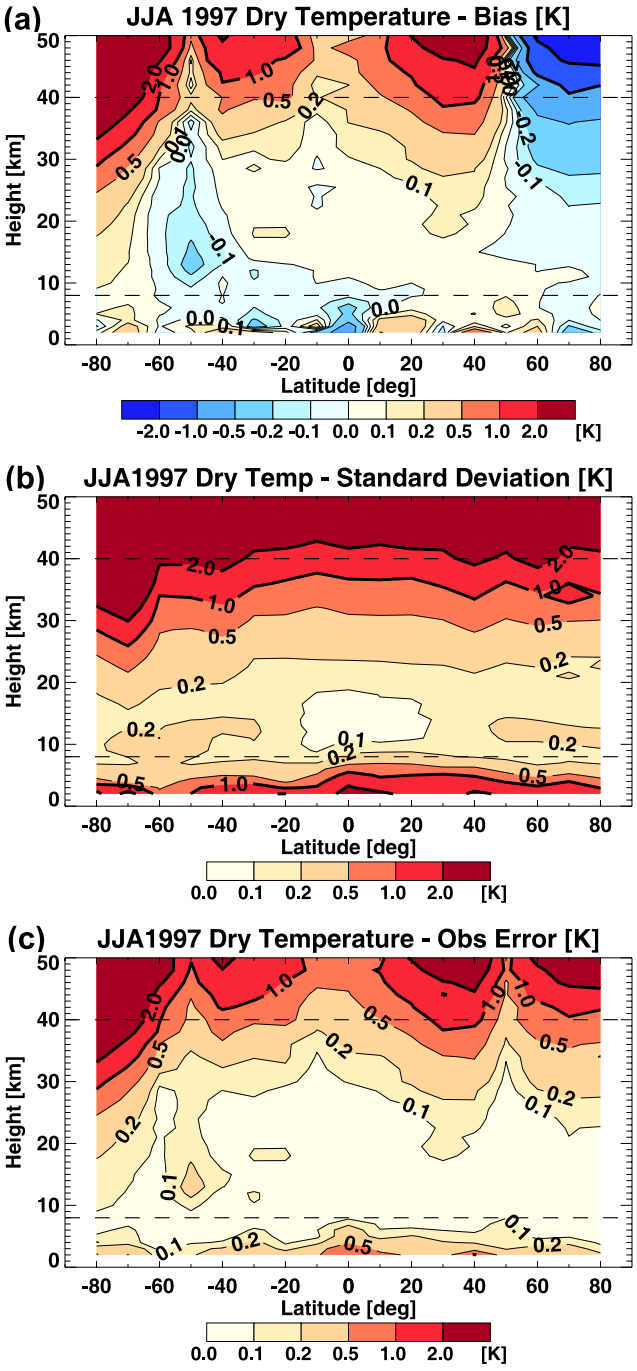

Figure 5. (a) Dry temperature bias, (b) standard deviation, and (c) observational error for the test bed season JJA 1997. The "core region" (8 to 40 km) is indicated by dashed lines. Systematic positive and negative differences of 0.1 K, 0.2 K, and 0.5 K, respectively, are drawn with light lines, differences of 1 K and 2 K, respectively, with heavy lines.

CHAMP and COSMIC. After subtraction of the estimated respective sampling error, seasonal temperature climatologies derived from different COSMIC satellites agree to within <0.1 K almost everywhere between 8 km and 35 km altitude. These results demonstrate the consistency of RO data from different satellites, but common systematic errors, which would cancel when computing systematic differences, cannot be ruled out. The results of the present study provide further evidence, that ~0.1–0.2 K is a reasonable typical value for RO dry temperature systematic errors between 8 km and 30 km altitude.

[45] Regarding the long-term stability of such potential residual biases, we have currently no evidence or knowledge of processes in homogenously processed RO data that would significantly change over time [*Steiner et al.*, 2007], i.e., the data might be essentially free of time-varying biases as they nominally should be based on the self-calibration principle (section 2.2). The full 25-year OSSE study as well as future intercomparison of trends in real multiyear RO data records of independent processing centers, and traceback to the international time standard [*Leroy et al.*, 2006a], are planned to help quantify potential residual bias drifts.

[46] The dry temperature standard deviations for the test bed season are shown in Figure 5b. The best results (with values generally below 0.5 K) are achieved at altitudes between ~7 km and ~30 km altitude. Below and above the general feature is a steady increase of errors with decreasing/increasing height. Standard deviations of 2 K are reached around 2 km and 40 km altitude, respectively. Standard deviations in the two southernmost bins are only slightly larger. The mean standard deviation in the core region is 0.54 K (0.41 K in the Northern Hemisphere). Horizontal variability (the part not included in T42 horizontal resolution) would further increase standard deviation but above about 7 km height only by a small amount of ~0.2 K [*Foelsche and Kirchengast*, 2004]. Consistent with this as an upper bound, estimates of *Kuo et al.* [2004] and *Steiner et al.* [2006] for real RO data suggest that RO-attributable temperature standard deviations are <1 K within 10–30 km.

[47] The observational error of the dry temperature climatologies is given by the root mean square error (RMS) of the mean. For each altitude level in each bin, the observational dry temperature error, $\Delta T_{\mathrm{dry}}^{\mathrm{obs}}$, is a combination of the systematic error of the mean, $\Delta T_{\mathrm{dry}}^{\mathrm{bias}}$, and the standard deviation of the mean:

$$\Delta T_{\mathrm{dry}}^{\mathrm{obs}} = \left[\left(\Delta T_{\mathrm{dry}}^{\mathrm{bias}} \right)^2 + \left(\frac{\Delta T_{\mathrm{dry}}^{\mathrm{stddev}}}{\sqrt{N_{\mathrm{prof}}}} \right)^2 \right]^{1/2}, \qquad (2)$$

where $\Delta T_{\mathrm{dry}}^{\mathrm{stddev}}$ is the standard deviation of the ensemble of N_{prof} profiles for the respective matrix element.

[48] The observational error for the test bed season is displayed in Figure 5c and evidently dominated by the systematic component (Figure 5a). Even at 40 km altitude, where the standard deviations are ~2 K, the error reduction by a factor of ~7 (second term at the right hand side of equation (2)) leads to a standard deviation of the mean <0.3 K. Figure 5c is therefore closely similar to the absolute bias (obtained if taking the absolute values of Figure 5a); typical observational errors are only of order 0.01 K larger than the corresponding absolute biases. The mean observational error in the core region is 0.22 K (0.16 K in the Northern Hemisphere). The dominance of the systematic error in the observational error, due to the strong reduction of the statistical error by averaging, also holds for real RO data for any reasonable number of events per bin of order 100 events [*Foelsche et al.*, 2007].

4.4. Sampling Error

[49] In addition to the observational error, we have to consider the sampling or representativity error, also known as under-sampling, when we attempt to build climatologies from satellite data [e.g., *Salby and Callaghan*, 1997; *Leroy*, 2001; *Mears and Wentz*, 2005; *Kirk-Davidoff et al.*, 2005]. Even with perfect observations the measured climatologies would differ from the "true" ones as the sampling through RO profiles is discrete and not dense enough to capture the entire spatial and temporal variability of the atmosphere. In the framework of our OSSE, perfect observations are available in form of the "true" GCM profiles at the locations of the RO events. We can therefore estimate the sampling error by comparing climatologies derived from the GCM profiles at the RO locations with climatologies derived from using the complete GCM field (practically sampled for the purpose with 1° lat/lon spacing). The dry temperature sampling error profile in each bin is thus estimated as:

$$\Delta T_{\mathrm{dry}}^{\mathrm{sampling}}(z) = \frac{1}{N_{\mathrm{prof}}} \sum_{i=1}^{N_{\mathrm{prof}}} T_{\mathrm{dry}_i}^{\mathrm{true}}(z) - \frac{1}{N_{\mathrm{grid}}} \sum_{j=1}^{N_t} \sum_{k=1}^{N_\varphi} \sum_{l=1}^{N_\lambda} T_{\mathrm{dry}_{jkl}}^{\mathrm{true}}(z), \qquad (3)$$

where N_{prof} is the number of profiles in the bin, the summation on the right hand side is over all N_λ longitude and N_φ latitude grid points in the bin and over all N_t time layers within the selected time interval, $N_{\mathrm{grid}} = N_\lambda\, N_\varphi\, N_t$. Cosine weighting (equation (1)) and decrease of ensemble members with decreasing height (section 4.1) are taken into account but are not explicitly written in equation (3) for the sake of simplicity.

[50] The sampling error for the JJA 1997 season, using the selected ~1000 events, is shown in Figure 6a. The most prominent feature is a large positive sampling error at high southern latitudes (centered at around 60°S), due to incomplete sampling of the edge of the austral polar vortex, where the latitudinal dry temperature gradient is large (see Figure 4). The plot is quite structured, but we preferred to use for consistency the same contour spacing as in the other plots. As the sampling error can be positive and negative, it is again required to use absolute values to indicate typical errors. The mean absolute sampling error in the core region is 0.36 K (0.22 K in the Northern Hemisphere).

[51] The sampling error for the full ensemble of ~13,000 events can be estimated without performing the full forward-inverse simulation (i.e., it is no computing time challenge), since only the RO event locations are required for the estimation of the sampling error. The results are shown in Figure 6b. The overall structure is quite similar, largest errors occur again at high southern latitudes. The error reduction is clearly visible but definitely smaller than what one might intuitively expect given an increase of the number of RO events by a factor of ~13. "Additional" RO events frequently occur in close spatial and temporal vicinity to existing ones, which therefore do not markedly

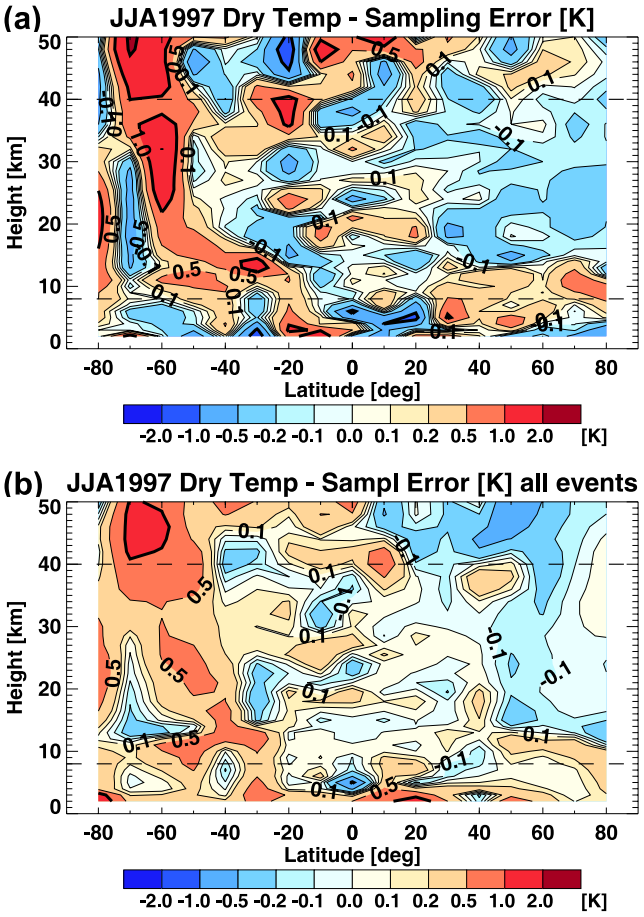

Figure 6. Dry temperature sampling error for the test bed season JJA 1997: (a) using the selected ~1000 events and (b) using all ~13,000 events.

improve the sampling situation. In the original data set there are up to 15 RO events per bin and 6 h time layer, in the subset there is at most one. The mean absolute sampling error for all events in the core region is 0.22 K (0.13 K in the Northern Hemisphere), less than a factor two smaller than the sampling error for the subset of ~1000 events. This shows, on the other hand, that the subset was well selected. Even when taking all available events, the sampling error has the same magnitude as the observational error. In case of actual RO climatologies, even from single satellites, the sampling error can easily be reduced by building larger area means, e.g., zonal means. As an example, the typical sampling error in the UTLS for seasonal and zonal mean climatologies (10° latitude bands) derived from CHAMP RO data is <0.2 K [*Foelsche et al.*, 2007; *Pirscher et al.*, 2007].

4.5. Climatological Error

[52] The total climatological error, $\Delta T_{\mathrm{dry}}^{\mathrm{clim}}$, is a combination of the observational error (equation (2)) and the sampling error (equation (3)). As these two error sources can be assumed uncorrelated we obtain:

$$\Delta T_{\mathrm{dry}}^{\mathrm{clim}} = \left[\left(\Delta T_{\mathrm{dry}}^{\mathrm{obs}} \right)^2 + \left(\Delta T_{\mathrm{dry}}^{\mathrm{sampling}} \right)^2 \right]^{1/2}. \qquad (4)$$

[53] Figure 7a shows the climatological error for the test bed season, the mean value in the core region is 0.49 K (0.32 K in the Northern Hemisphere). In a considerable part of the core region the climatological error is <0.2 K. South of 50°S, however, the coincidence of large observational and sampling errors leads to total errors of 1 to 2 K, indicating that high latitude winter areas can be a challenging region for RO based climatologies with comparatively high horizontal resolution. Above ~40 km height the total error increases markedly, reaching values of 2 to 4 K.

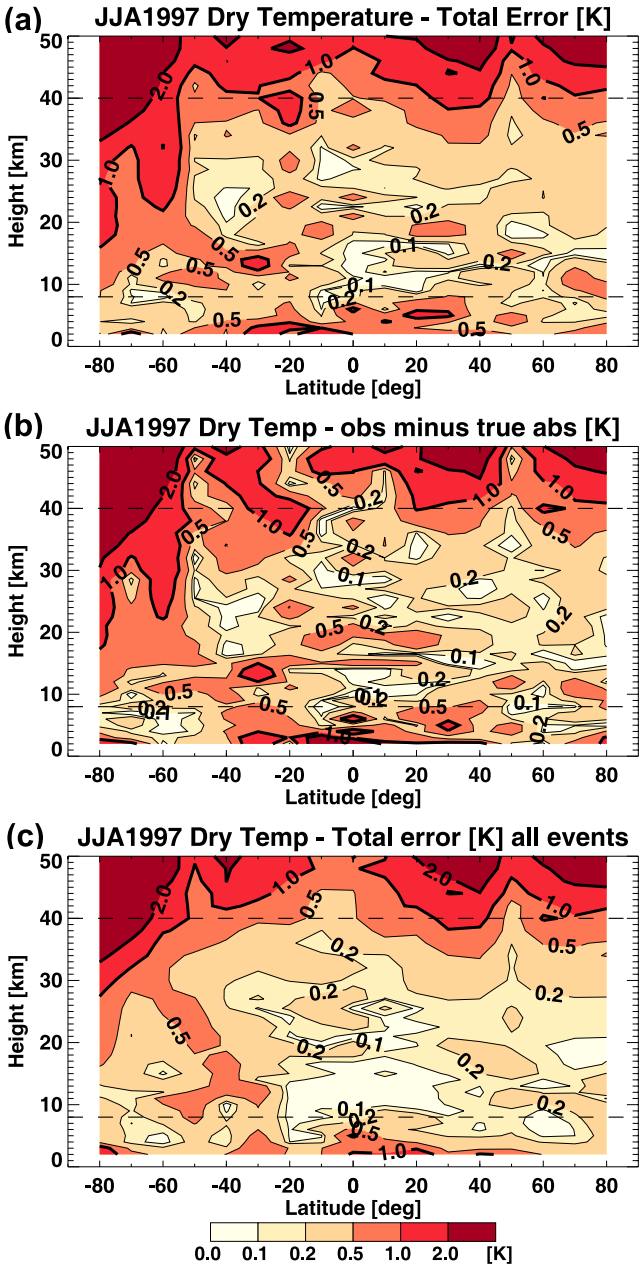

Figure 7. Climatological error for the test bed season JJA 1997: (a) climatological dry temperature error, (b) absolute values for the difference between the "observed" and the "true" dry temperature climatology, and (c) estimated climatological dry temperature error using all ~13,000 events for sampling error estimation.

[54] In an OSSE with the "true" field available, we have another way to look at the total climatological error, simply by computing the difference between the "observed" climatology (Figure 4a) and the "true" climatology (Figure 4b). The absolute values of this difference should be very close to the results of the approach introduced above, where only positive values are possible due to the component computations involved (equations (2) to (4)). This is clearly the case as can be seen in Figure 7b; the mean absolute observed-minus-true error in the core region is 0.47 K (0.30 K in the Northern hemisphere), 0.02 K smaller then the climatological error via equation (4). We can therefore also estimate the climatological error for the full ensemble of ~13,000 events, under the reasonable assumption that the bias of the subset of ~1000 events is also representative for the full ensemble. Applying equation (4) to the observational error of the subset and the sampling error of the full ensemble yields the results shown in Figure 7c. The estimated mean climatological error for all events in the core region is 0.36 K (0.24 K in the Northern Hemisphere). Particularly small errors (<0.1 K) are found in the upper troposphere at low (tropical) latitudes.

5. Trends in Atmospheric Parameters

[55] To put the climatological errors estimated in the test bed study for a typical seasonal mean JJA field into perspective, we show the temperature trends over the period 2001–2025 as simulated with the MAECHAM5 model with anthropogenic forcings (section 3.1). Figure 8a shows the temperature trends per decade for the geographic domain used in this study (Figure 2a), on the 17 × 34 grid described in section 4.2. A salient feature, which is only partly visible in "normal" climate model runs with a vertical domain up to the 10 hPa level (30–35 km) [e.g., *IPCC*, 2007], is the pronounced cooling in the stratosphere. Given the accuracy of RO data in the lower stratosphere it is thus possible that "stratospheric cooling" will be the first consequence of anthropogenic climate change that can be detected with the aid of the RO technique. On the other hand, the largest positive temperature trends, with values up to 0.6 K per decade, are expected below the tropical tropopause, where favorably the RO errors are particularly small (see Figure 7). Generally, in important parts of the core region the projected temperature trends per decade are at least twice as large as the climatological error of the RO climatologies. A detailed analysis can only be performed based on the results of the full 25-year experiment, which includes time dependence of errors, but already the present results indicate that temperature trends in important parts of the UTLS do have a fair chance to be detected in RO climatologies within a timeframe of 10 to 20 years. This is consistent with the conclusions of *Leroy et al.* [2006b] who find that RO data should allow detecting climate trends within about 10 years. We have thus in parallel started a study on temperature trend detection in the UTLS, using GPS/MET RO data from 1995 and 1997 combined with CHAMP RO data from 2001–2007, with the trends tested versus natural variability estimated from multi-century climate model control runs.

[56] It is also very interesting to look at other climate variables that can be observed with the RO technique [*Foelsche et al.*, 2006]. Along this line, trends in pressure and microwave refractivity are shown in Figures 8b and 8c, respectively. Given the exponential decrease of both parameters with increasing height, and the large dynamic range of the absolute values, we inspect relative trends per decade in these cases (with the year 2001 taken as basis). Note that relative pressure trends are proportional to absolute geopotential height trends, where the proportionality factor is the local scale height [*Leroy et al.*, 2006a, 2006b]. Thus

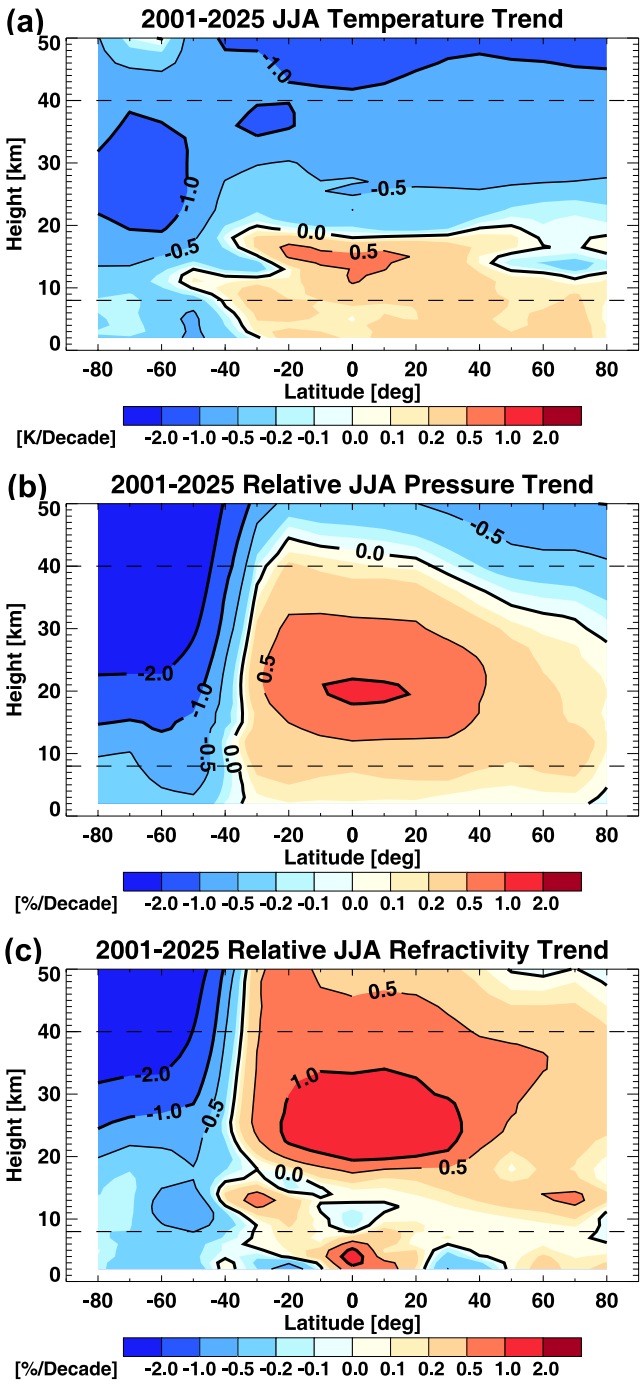

Figure 8. MAECHAM5 trend results for 2001–2025 (anthropogenically forced run): (a) temperature trend per decade, (b) relative pressure trend per decade, and (c) relative refractivity trend per decade.

Figure 8b represents also geopotential height trends. For example, the pressure trend of ~0.5%/decade near 12 km in the tropical upper troposphere (UT) implies a geopotential height trend of ~32 m/decade (assuming a scale height ~6.5 km), indicating that the 200 hPa pressure level is raised by this amount due to the warming of the tropical troposphere underneath.

[57] When we compare the results for the three climate variables in Figures 8a–8c, we see salient changes in each parameter, but in different parts of the latitude-height domain. For example in the low latitude UTLS, the largest positive temperature trend occurs near 15 km altitude, the largest relative pressure trend near 20 km, and the largest relative refractivity trend near 25 km, respectively. These trend behaviors are largely consistent with the ones shown by *Leroy et al.* [2006a] based on CMIP2+ (Coupled Model Intercomparison Project) models [*Covey et al.*, 2003], and by *Leroy et al.* [2006b] based on IPCC Fourth Assessment Report (AR4) Models [*IPCC*, 2007], respectively. Regarding the stratosphere above 30 km, the limitations of the CMIP2+ and IPCC AR4 model fields, top-limited by the 10 hPa level instead of the 0.01 hPa level of the fields here, are evident, however.

[58] An interesting feature of Figure 8c is the markedly small change in refractivity in the tropical UT (<0.1–0.2%/decade). Microwave refractivity N is related to temperature T, total pressure p, and water vapor partial pressure e, via [*Smith and Weintraub*, 1953]:

$$N \equiv 10^6(n-1) = k_1 \frac{p}{T} + k_2 \frac{e}{T^2}, \tag{5}$$

where n is the index of refraction, k_1 is 77.6 K/hPa, and k_2 is $3.73 \cdot 10^5$ K^2/hPa. When atmospheric humidity is small (valid at >10 km), the second term on the right-hand-side of equation (5) can be disregarded. We immediately see that in this case the same relative increase in T and p, which is approximately true in the tropical UT, will result in no change in refractivity. The key message of Figure 8 is that different RO-accessible atmospheric parameters are sensitive in different regions of the atmosphere. RO based climate monitoring should therefore carefully exploit all parameters that can be retrieved with the RO technique in order to optimize sensitivity to climate change.

6. Summary, Conclusions, and Outlook

[59] We currently perform a climate observing system simulation experiment (OSSE), where we analyze the climate change detection capability of a GNSS RO observing system. We focus on the atmospheric temperature change detection capability based on quasi-realistic end-to-end simulations over the 25 year period from 2001 to 2025.

[60] Here we described the setup of this climate OSSE and the results of a test bed study to carefully characterize the RO climatology errors of relevance, systematic and statistical observational errors as well as sampling errors, for the JJA seasonal means considered. The OSSE involves atmosphere modeling using the MAECHAM5 T42L39 GCM model and ionosphere modeling using the NeUoG model. RO observables for a small six-satellite GNSS receiver constellation are simulated, based on ray tracing through the atmospheric and ionospheric fields. The simulated RO phase delay profiles show the error characteristics of modern GNSS occultation receivers as well as reasonable ionospheric residual errors. A state-of-the-art retrieval processing chain is used for (dry) atmospheric profiles retrieval from the phase delay data.

[61] The test bed results, obtained for JJA 1997 as a typical summer season, on observational errors and sampling errors were found encouraging for performing the full 25-year experiment, since we found projected temperature trends per decade from the MAECHAM5 anthropogenically forced model run in parts of the UTLS to be at least twice as large as the total errors of the RO climatologies. This indicates, for example, that temperature trends in the tropical upper troposphere should be reliably detectable based on RO climatologies within a timeframe of 10 to 20 years. We are thus in parallel conducting a study on temperature trend detection in the UTLS, using GPS/MET RO data from 1995 and 1997 combined with CHAMP RO data from 2001–2007, with the trends tested versus natural variability estimated from multicentury climate model control runs.

[62] Comparative inspection of the trend results from the MAECHAM5 forced run for different RO-accessible atmospheric parameters (refractivity and pressure/geopotential height in addition to temperature) reveals complementary climate change sensitivity of them to different regions of the UTLS. For optimal sensitivity, RO based climate monitoring should thus include all these parameters.

[63] After the observables simulations for all 25 years are complete, trends in both the "observed" climatology from the simulated RO events and the "true" climatology from the GCM modeling will be computed, for both the anthropogenic forcing and natural variability run, and interpreted by statistical analysis. Given the real RO climate record, mainly from CHAMP, being only 6 years long by 2007 (except for a few submonthly periods of reasonable quality from GPS/MET within 1995–1997), and being largely from periods of low solar activity, the analysis of the 25-year climate OSSE will for the first time allow us to quantitatively evaluate the potential long-term behavior of RO records over more than two decades and solar cycles.

[64] **Acknowledgments.** The authors thank A. Gobiet (WegCenter, Univ. of Graz) for valuable scientific discussions and the EGOPS software team (WegCenter and IGAM, Univ. of Graz) for their technical support. EGOPS development was mainly funded by the European Space Agency (ESA). The ECHAM model team at MPI-M Hamburg, Germany, is thanked for technical support in the climate model simulations. Funding for this work was received from the Austrian Science Fund (FWF) under the START research award of G. K. (Program Y103-N03). Additional partial support by funds of L. B. from MPI-M Hamburg is also gratefully acknowledged. We thank three anonymous reviewers for their constructive and helpful comments.

References

Anthes, R. A., C. Rocken, and Y.-H. Kuo (2000), Applications of COSMIC to meteorology and climate, *Terr. Atmos. Oceanic. Sci.*, *11*, 115–156.

Bengtsson, L., E. Roeckner, and M. Stendel (1999), Why is the global warming proceeding much slower than expected?, *J. Geophys. Res.*, *104*(D4), 3865–3876.

Bengtsson, L., S. Hagemann, and K. I. Hodges (2004), Can climate trends be calculated from reanalysis data?, *J. Geophys. Res.*, *109*, D11111, doi:10.1029/2004JD004536.

Borsche, M., G. Kirchengast, and U. Foelsche (2007), Tropical tropopause climatology as observed with radio occultation measurements from

CHAMP compared to ECMWF and NCEP analyses, *Geophys. Res. Lett.*, *34*, L03702, doi:10.1029/2006GL027918.

Christy, J. R., and R. W. Spencer (2003), Reliability of satellite data sets, *Science*, *301*, 1046–1047.

Covey, C., K. M. Achuta-Rao, U. Cubasch, P. Jones, S. J. Lambert, M. E. Mann, T. J. Phillips, and K. E. Taylor (2003), An overview of results from the Coupled Model Intercomparison Project, *Global Planet. Change*, *37*(1–2), 103–133.

Fjeldbo, G., A. J. Kliore, and V. R. Eshleman (1971), The neutral atmosphere of Venus as studied with the Mariner V radio occultation experiments, *Astron. J.*, *76*, 123–140.

Foelsche, U., and G. Kirchengast (2004), Sensitivity of GNSS radio occultation data to horizontal variability in the troposphere, *Phys. Chem. Earth*, *29*(2–3), 225–240, doi:10.1016/j.pce.2004.01.007.

Foelsche, U., G. Kirchengast, and A. K. Steiner (2003), Global climate monitoring based on CHAMP/GPS radio occultation data, in *First CHAMP Mission Results for Gravity, Magnetic and Atmospheric Studies*, edited by C. Reigber et al., pp. 397–407, Springer, New York.

Foelsche, U., A. Gobiet, A. Löscher, G. Kirchengast, A. K. Steiner, J. Wickert, and T. Schmidt (2005), The CHAMPCLIM project: An overview, in *Earth Observation With CHAMP – Results From Three Years in Orbit*, edited by C. Reigber et al., pp. 615–620, Springer, New York, doi:10.1007/3-540-26800-6_98.

Foelsche, U., A. Gobiet, A. K. Steiner, M. Borsche, J. Wickert, T. Schmidt, and G. Kirchengast (2006), Global climatologies based on radio occultation data: The CHAMPCLIM project, in *Atmosphere and Climate: Studies by Occultation Methods*, edited by U. Foelsche, G. Kirchengast, and A. K. Steiner, pp. 303–314, Springer, New York, doi:10.1007/3-540-34121-8_25.

Foelsche, U., M. Borsche, A. K. Steiner, A. Gobiet, B. Pirscher, and G. Kirchengast (2007), Observing upper troposphere-lower stratosphere climate with radio occultation data from the CHAMP satellite, *Clim. Dyn.*, doi:10.1007/s00382-007-0337-7.

Foelsche, U., B. Pirscher, M. Borsche, G. Kirchengast, and J. Wickert (2008), Assessing the climate monitoring utility of radio occultation data: From CHAMP to FORMOSAT-3/COSMIC, *Terr. Atmos. Oceanic Sci.*, in press.

Fu, Q., C. M. Johanson, S. G. Warren, and D. J. Seidel (2004), Contribution of stratospheric cooling to satellite-inferred tropospheric temperature trends, *Nature*, *429*, 55–58.

Giorgetta, M. A., E. Manzini, E. Roeckner, M. Esch, and L. Bengtsson (2006), Climatology and forcing of the quasi-biennial oscillation in the MAECHAM5 model, *J. Clim.*, *19*, 3882–3901.

Gobiet, A., and G. Kirchengast (2004), Advancements of GNSS radio occultation retrieval in the upper stratosphere for optimal climate monitoring utility, *J. Geophys. Res.*, *109*, D24110, doi:10.1029/2004JD005117.

Gobiet, A., U. Foelsche, A. K. Steiner, M. Borsche, G. Kirchengast, and J. Wickert (2005), Climatological validation of stratospheric temperatures in ECMWF operational analyses with CHAMP radio occultation data, *Geophys. Res. Lett.*, *32*, L12806, doi:10.1029/2005GL022617.

Gobiet, A., G. Kirchengast, G. L. Manney, M. Borsche, C. Retscher, and G. Stiller (2007), Retrieval of temperature profiles from CHAMP for climate monitoring: Intercomparison with Envisat MIPAS and GOMOS and different atmospheric analyses, *Atmos. Chem. Phys.*, *7*, 3519–3536.

Gorbunov, M. E. (2002), Canonical transform method for processing radio occultation data in the lower troposphere, *Radio Sci.*, *37*(5), 1076, doi:10.1029/2000RS002592.

Gorbunov, M. E., and K. B. Lauritsen (2004), Analysis of wave fields by Fourier integral operators and their application for radio occultations, *Radio Sci.*, *39*, RS4010, doi:10.1029/2003RS002971.

Hajj, G. A., E. R. Kursinski, L. J. Romans, W. I. Bertiger, and S. S. Leroy (2002), A technical description of atmospheric sounding by GPS occultation, *J. Atmos. Sol. Terr. Phys.*, *64*, 451–469.

Hajj, G. A., C. O. Ao, B. A. Iijima, D. Kuang, E. R. Kursinski, A. J. Mannucci, T. K. Meehan, L. J. Romans, M. de la Torre Juarez, and T. P. Yunck (2004), CHAMP and SAC-C atmospheric occultation results and intercomparisons, *J. Geophys. Res.*, *109*, D06109, doi:10.1029/2003JD003909.

Hedin, A. E. (1991), Extension of the MSIS thermosphere model into the middle and lower amosphere, *J. Geophys. Res.*, *96*(A2), 1159–1172.

Hoeg, P., and G. Kirchengast (2002), ACE+ – Atmosphere and climate explorer based on GPS, GALILEO, and LEO-LEO radio occultation (ESA Earth Explorer Opportunity Mission proposal), in *Wissenschaftl. Ber.*, vol. 14, 121 pp., Inst. for Geophys., Astrophys., and Meteorol., Univ. of Graz, Austria.

IPCC (2001), *Climate Change 2001: The Scientific Basis. Contribution of Working Group I to the Third Assessment Report of the Intergovernmental Panel on Climate Change*, edited by J. T. Houghton et al., 881 pp., Cambridge Univ. Press, New York.

IPCC (2007), *Climate Change 2007: The Physical Science Basis. Contribution of Working Group I to the Fourth Assessment Report of the Intergovernmental Panel on Climate Change*, edited by S. Solomon et al., 996 pp., Cambridge Univ. Press, New York.

Jensen, A. S., M. S. Lohmann, H.-H. Benzon, and A. S. Nielsen (2003), Full Spectrum Inversion of radio occultation signals, *Radio Sci.*, *38*(3), 1040, doi:10.1029/2002RS002763.

Karl, T. R., S. J. Hassol, C. D. Miller, and W. L. Murray (Eds.) (2006), Temperature trends in the lower atmosphere: Steps for understanding and reconciling differences, in *A Report by the Climate Change Science Program and the Subcommittee on Global Change Research*, 164 pp., US Climate Change Science Program, Washington, D.C.

Kirchengast, G., A. K. Steiner, U. Foelsche, L. Kornblueh, E. Manzini, and L. Bengtsson (2000), Spaceborne climate change monitoring by GNSS occultation sensors, in *Proc. 11th Symp. Global Change Studies*, pp. 62–65, AMS Ann. Meeting 2000, Long Beach, Calif.

Kirchengast, G., J. Fritzer, and J. Ramsauer (2002), End-to-end GNSS Occultation Performance Simulator Version 4 (EGOPS4) Software User Manual (Overview and Reference Manual), in *Techn. Report for ESA/ESTEC* No. 3/2002, 472 pp., Inst. for Geophys., Astrophys., and Meteorol., Univ. of Graz, Austria.

Kirk-Davidoff, D., R. M. Goody, and J. G. Anderson (2005), Analysis of sampling errors for climate monitoring satellites, *J. Clim.*, *18*, 810–822, doi:10.1175/JCLI-3301.1.

Kuo, Y.-H., T.-K. Wee, S. Sokolovskiy, C. Rocken, W. Schreiner, D. Hunt, and R. A. Anthes (2004), Inversion and error estimation of GPS radio occultation data, *J. Meteorol. Soc. Jpn.*, *82*, 507–531.

Kursinski, E. R., G. A. Hajj, J. T. Schofield, R. P. Linfield, and K. R. Hardy (1997), Observing Earth's atmosphere with radio occultation measurements using GPS, *J. Geophys. Res.*, *102*(D19), 23,429–23,465.

Leitinger, R., and G. Kirchengast (1997), Inversion of the plasma signal in GNSS occultations – Simulation studies and sample results, *Acta Geod. Geophys. Hung.*, *32*, 379–394.

Leitinger, R., J. E. Titheridge, G. Kirchengast, and W. Rothleitner (1996), A "simple" global empirical model for the F layer of the ionosphere, *Kleinheubacher Ber.*, *39*, 697–704 (in German; English version available from the authors).

Leroy, S. S. (2001), The effects of orbital precession on remote climate monitoring, *J. Clim.*, *14*, 4330–4337, doi:10.1175/1520-0442(2001)014<4330:TEOOPO>2.0.CO;2.

Leroy, S. S., and J. R. North (2000), The application of COSMIC data to global change research, *Terr. Atmos. Oceanic Sci.*, *11*(1), 187–210.

Leroy, S., J. A. Dykema, and J. G. Anderson (2006a), Climate benchmarking using GNSS occultation, in *Atmosphere and Climate: Studies by Occultation Methods*, edited by U. Foelsche, G. Kirchengast, and A. K. Steiner, pp. 287–301, Springer, New York, doi:10.1007/3-540-34121-8_24.

Leroy, S. S., J. G. Anderson, and J. A. Dykema (2006b), Testing climate models using GPS radio occultation: A sensitivity analysis, *J. Geophys. Res.*, *111*, D17105, doi:10.1029/2005JD006145.

Liou, Y.-A., A. G. Pavelyev, S. F. Liu, A. A. Pavelyev, N. Yen, C. Y. Huang, and C. J. Fong (2007), FORMOSAT-3 GPS radio occultation mission: Preliminary results, *IEEE Trans. Geosci. Remote Sens.*, *45*(10), doi:10.1109/TGRS.2007.903365.

Loiselet, M., N. Stricker, Y. Menard, and J.-P. Luntama (2000), GRAS – MetOp's GPS-based atmospheric sounder, *ESA Bull.*, *102*, 38–44.

Luntama, J.-P. (2006), The operational EPS GRAS measurement system, in *Atmosphere and Climate: Studies by Occultation Methods*, edited by U. Foelsche, G. Kirchengast, and A. K. Steiner, pp. 147–156, Springer, New York.

Manzini, E., and N. A. McFarlane (1998), The effect of varying the source spectrum of a gravity wave parameterization in a middle atmosphere general circulation model, *J. Geophys. Res.*, *103*(D24), 31,523–31,539.

Manzini, E., N. A. McFarlane, and C. McLandress (1997), Impact of the Doppler spread parameterization on the simulation of the middle atmosphere circulation using the MA/ECHAM4 general circulation model, *J. Geophys. Res.*, *102*(D22), 25,751–25,762.

Manzini, E., M. A. Giorgetta, M. Esch, L. Kornblueh, and E. Roeckner (2006), The influence of sea surface temperatures on the Northern winter stratosphere: Ensemble simulations with the MAECHAM5 model, *J. Clim.*, *19*, 3863–3881.

Mears, C. A., and F. J. Wentz (2005), The effect of drifting measurement time on satellite-derived lower tropospheric temperature, *Science*, *309*, 1548–1551.

Mears, C., M. Schabel, and F. J. Wentz (2003), A reanalysis of the MSU channel 2 tropospheric temperature record, *J. Clim.*, *16*, 3650–3664.

Pavelyev, A. G., Y. A. Liou, J. Wickert, T. Schmidt, A. A. Pavelyev, and S. F. Liu (2007), Effects of the ionosphere and solar activity on radio

occultation signals: Application to CHAllenging Minisatellite Payload satellite observations, *J. Geophys. Res.*, *112*, A06326, doi:10.1029/2006JA011625.

Pirscher, B., U. Foelsche, B. C. Lackner, and G. Kirchengast (2007), Local time influence in single-satellite radio occultation climatologies from Sun-synchronous and non Sun-synchronous satellites, *J. Geophys. Res.*, *112*, D11119, doi:10.1029/2006JD007934.

Rocken, C., et al. (1997), Analysis and validation of GPS/MET data in the neutral atmosphere, *J. Geophys. Res.*, *102*(D25), 29,849–29,866.

Rocken, C., Y.-H. Kuo, W. S. Schreiner, D. Hunt, S. Sokolovskiy, and C. McCormick (2000), COSMIC system description, *Terr. Atmos. Oceanic Sci.*, *11*(1), 21–52.

Roeckner, E., L. Bengtsson, J. Feichter, J. Lelieveld, and H. Rodhe (1999), Transient climate change simulations with a coupled atmosphere-ocean GCM including the tropospheric sulfur cycle, *J. Clim.*, *12*, 3004–3032.

Salby, M. L., and P. Callaghan (1997), Sampling error in climate properties derived from satellite measurements: Consequences of undersampled diurnal variability, *J. Clim.*, *10*, 18–36.

Schmidt, T., S. Heise, J. Wickert, G. Beyerle, and C. Reigber (2005), GPS radio occultation with CHAMP and SAC-C: Global monitoring of thermal tropopause parameters, *Atmos. Chem. Phys.*, *5*, 1473–1488.

Schmidt, T., G. Beyerle, S. Heise, J. Wickert, and M. Rothacher (2006), A climatology of multiple tropopauses derived from GPS radio occultations with CHAMP and SAC-C, *Geophys. Res. Lett.*, *33*, L04808, doi:10.1029/2005GL024600.

Schreiner, W., C. Rocken, S. Sokolovskiy, S. Syndergaard, and D. Hunt (2007), Estimates of the precision of GPS radio occultations from the COSMIC/FORMOSAT-3 mission, *Geophys. Res. Lett.*, *34*, L04808, doi:10.1029/2006GL027557.

Schrøder, T., S. Leroy, M. Stendel, and E. Kaas (2003), Validating the microwave sounding unit stratospheric record using GPS occultation, *Geophys. Res. Lett.*, *30*(14), 1734, doi:10.1029/2003GL017588.

Seidel, D. J., et al. (2004), Uncertainty in signals of large-scale climate variations in radiosonde and satellite upper-air temperature datasets, *J. Clim.*, *17*, 2225–2240.

Sherwood, S. C., J. R. Lanzante, and C. L. Meyer (2005), Radiosonde daytime biases and late-20th century warming, *Science*, *309*, 1556–1559.

Smith, E. K., and S. Weintraub (1953), The constants in the equation for atmospheric refractive index at radio frequencies, *Proc. IRE*, *41*, 1035–1037.

Steiner, A. K., and G. Kirchengast (2005), Error analysis for GNSS radio occultation data based on ensembles of profiles from end-to-end simulations, *J. Geophys. Res.*, *110*, D15307, doi:10.1029/2004JD005251.

Steiner, A. K., G. Kirchengast, and H. P. Ladreiter (1999), Inversion, error analysis, and validation of GPS/MET occultation data, *Ann. Geophys.*, *17*, 122–138.

Steiner, A. K., G. Kirchengast, U. Foelsche, L. Kornblueh, E. Manzini, and L. Bengtsson (2001), GNSS occultation sounding for climate monitoring, *Phys. Chem. Earth Part A*, *26*, 113–124.

Steiner, A. K., A. Loescher, and G. Kirchengast (2006), Error characteristics of refractivity profiles retrieved from CHAMP radio occultation data, in *Atmosphere and Climate: Studies by Occultation Methods*, edited by U. Foelsche, G. Kirchengast, and A. K. Steiner, pp. 27–36, Springer, New York, doi:10.1007/3-540-34121-8_3.

Steiner, A. K., G. Kirchengast, M. Borsche, U. Foelsche, and T. Schoengassner (2007), A multi-year comparison of lower stratospheric temperatures from CHAMP radio occultation data with MSU/AMSU records, *J. Geophys. Res.*, *112*, D22110, doi:10.1029/2006JD008283.

Syndergaard, S. (1999), Retrieval analysis and methodologies in atmospheric limb sounding using the GNSS radio occultation technique, *DMI Sci. Rep. 99-6*, 131 pp., Danish Met. Inst., Copenhagen, Denmark, available at http://www.dmi.dk/dmi/sr99-6.pdf.

Thorne, P. W., D. E. Parker, J. R. Christy, and C. A. Mears (2005), Uncertainties in climate trends: Lessons from upper-air temperature records, *Bull. Am. Meteor. Soc.*, *86*, 1437–1442.

Trenberth, K. E., et al. (2007), Observations: Surface and atmospheric climate change, in *Climate Change 2007: The Physical Science Basis. Contribution of Working Group I to the Fourth Assessment Report of the Intergovernmental Panel on Climate Change*, edited by S. Solomon et al., pp. 235–336, Cambridge Univ. Press, New York.

Vinnikov, K. Y., and N. C. Grody (2003), Global warming trend of mean tropospheric temperature observed by satellites, *Science*, *302*, 269–272.

Vinnikov, K. Y., N. C. Grody, A. Robock, R. J. Stouffer, P. D. Jones, and M. D. Goldberg (2006), Temperature trends at the surface and in the troposphere, *J. Geophys. Res.*, *111*, D03106, doi:10.1029/2005JD006392.

Vorob'ev, V. V., and T. G. Krasil'nikova (1994), Estimation of the accuracy of the atmospheric refractive index recovery from Doppler shift measurements at frequencies used in the NAVSTAR system, *Phys. Atmos. Ocean*, *29*, 602–609.

Ware, R., et al. (1996), GPS Sounding of the atmosphere from Low Earth Orbit: Preliminary results, *Bull. Am. Meteorol. Soc.*, *77*, 19–40.

Wickert, J., T. Schmidt, G. Beyerle, R. König, C. Reigber, and N. Jakowski (2004), The radio occultation experiment aboard CHAMP: Operational data analysis and validation of vertical atmospheric profiles, *J. Meteorol. Soc. Jpn.*, *82*, 381–395.

Wu, B.-H., V. Chu, P. Chen, and T. King (2005), FORMOSAT-3/COSMIC science mission update, *GPS Solut.*, *9*, 111–121, doi:10.1007/s10291-005-0140-z.

Yuan, L. L., R. A. Anthes, R. H. Ware, C. Rocken, W. D. Bonner, M. G. Bevis, and S. Businger (1993), Sensing climate change using the global positioning system, *J. Geophys. Res.*, *98*(D8), 14,925–14,937.

Yunck, T. P., C. Liu, and R. Ware (2000), A history of GPS sounding, *Terr. Atmos. Oceanic Sci.*, *11*(1), 1–20.

L. Bengtsson and L. Kornblueh, Max-Planck-Institute for Meteorology (MPI-M), Bundesstr. 53, D-20146 Hamburg, Germany.

U. Foelsche, G. Kirchengast, and A. K. Steiner, Wegener Center for Climate and Global Change (WegCenter), University of Graz, Leechgasse 25, A-8010 Graz, Austria. (ulrich.foelsche@uni-graz.at)

E. Manzini, Istituto Nazionale di Geofisica e Vulcanologia (INGV) and Centro Euro-Mediterraneo per il Cambiamento Climatico, Via Donato Creti, I-40128 Bologna, Italy.